PAPER

Check for updates

A general strategy to enhance the electrochemical activity and energy density of energy-storage materials through using sintering aids with redox activity: a case study of $Mo_4Nb_{26}O_{77}$†

Songjie Li, Jiazhe Gao, Yinjun Ou, Wenze Wang, Qian Zhang, Shangfu Gao, Xuehua Liu and Chunfu Lin [ID] *

The solid-state reaction method for energy-storage material preparations is simple and cost effective, thereby being suitable for industrialization. However, its sintering temperatures are generally high, resulting in large-sized (>1 μm) primary particles with low electrochemical activity. Here, based on a $Mo_4Nb_{26}O_{77}$ model material, we explore a general modification of the solid-state reaction method through using sintering aids with redox activity and successfully prepare $Mo_4Nb_{26}O_{77}$ with submicron-sized (∼200 nm) primary particles at a low sintering temperature of only 700 °C. The resultant high electrochemical activity of $Mo_4Nb_{26}O_{77}$ and its additional Mo-based redox activity which originated from the MoO_3 sintering aid enable its large practical capacity of 366 mA h g^{-1}, which is the largest in the field of niobate anode materials. $Mo_4Nb_{26}O_{77}$ further exhibits a relatively low working potential since more Nb^{4+} ions are reduced to Nb^{3+} ions at low potentials. Additionally, $Mo_4Nb_{26}O_{77}$ has high rate performance and good cyclability when external Li^+ ions mainly occupy the interstices between the (010) crystallographic planes of its open and stable shear ReO_3 crystal structure. Good low-temperature electrochemical properties are also achieved as a result of the high electrochemical activity. Therefore, this anode material has great practicability for high-performance Li^+ storage.

Chunfu Lin received his BE and ME degrees in Materials Science and Engineering from Tsinghua University in 2005 and 2007, respectively. He received his PhD degree from the National University of Singapore in 2014. He is currently a full professor at Qingdao University. He has published >80 papers in peer-reviewed journals, including Advanced Energy Materials, Advanced Functional Materials,

Advanced Science, ACS Nano and Energy Storage Materials. He is taking charge of two research programs funded by the National Natural Science Foundation of China. His scientific research includes energy storage and conversion materials, especially concentrating on niobium-based anode materials for high-performance lithium-ion batteries.

Institute of Materials for Energy and Environment, School of Materials Science and Engineering, Qingdao University, Qingdao 266071, China. E-mail: linchunfu@qdu.edu.cn

Introduction

Metal-ion batteries, such as lithium-ion batteries (LIBs), are playing an increasingly important role in various small-scale devices and large-scale facilities.[1–6] Their energy-storage materials, such as niobates, can be prepared through conventional solid-state reaction methods and wet-chemical synthesis methods (solvothermal method, sol–gel method, electrospinning method, *etc.*).[7–9] The wet-chemical synthesis methods usually use expensive organometallic salts, and the resultant products generally show low tap densities. In contrast, the solid-state reaction method is simple and cost effective, thereby being more suitable for industrialization. However, the sintering temperatures for the solid-state reaction of the niobates are usually very high (>1000 °C), resulting in large-sized (>1 μm) primary niobate particles with low electrochemical activity.[10–16] Generally, the practical capacity is far smaller than the theoretical one since the $Nb^{4+} \leftrightarrow Nb^{3+}$ redox reaction is mild in niobate micron-sized particles. For instance, the practical capacity of titanium niobate ($TiNb_2O_7$) micron-sized particles is

This journal is © The Royal Society of Chemistry 2022

J. Mater. Chem. A, 2022, **10**, 19953–19962 | **19953**

281 mA h g^{-1}, which is up to 27.6% smaller than the theoretical capacity of $TiNb_2O_7$ (388 mA h g^{-1}).[17] Therefore, it is highly necessary to modify the solid-state reaction method in order to achieve energy-storage materials with not only high electrochemical activity but also high energy density.

In this regard, here, we explore a general modification of the solid-state reaction method through using sintering aids with redox activity. The niobate is selected as the model energy-storage material, and MoO_3 with a low melting point (795 °C) and Mo-based redox activity is selected as its sintering aid.[18] As a result, $Mo_4Nb_{26}O_{77}$ with submicron-sized (∼200 nm) primary particles is successfully prepared through the solid-state reaction at a low sintering temperature of only 700 °C. Apart from the Nb^{4+}/Nb^{5+} and Nb^{3+}/Nb^{4+} redox couples, the Mo^{5+}/Mo^{6+} and Mo^{4+}/Mo^{5+} couples are also active in $Mo_4Nb_{26}O_{77}$ within 3.0–0.8 V *vs.* Li/Li$^+$, leading to its large theoretical capacity of 399 mA h g^{-1}, which surpasses those of most niobate anode compounds. The high electrochemical activity and additional Mo-based redox couples in the $Mo_4Nb_{26}O_{77}$ submicron-sized particles enable a large practical capacity of up to 366 mA h g^{-1}. It is known that typical niobate micron-sized particles show average working potentials of 1.7–1.8 V,[19] avoiding lithium-dendrite formation and electrolyte reduction which carbon anode materials with very low working potentials suffer from.[20] However, these working potentials are overly high, obviously limiting the energy density of full cells with niobate anodes. In this work, fortunately, the average working potential of the $Mo_4Nb_{26}O_{77}$ submicron-sized particles is lowered to 1.59 V since more Nb^{4+} ions are reduced to Nb^{3+} ions at low potentials ranging from 1.5 V to 0.8 V. Consequently, both the larger practical capacity and the lower working potential enable a higher energy density of full cells with $Mo_4Nb_{26}O_{77}$ anodes.

The $Mo_4Nb_{26}O_{77}$ submicron-sized particles further exhibit a high initial coulombic efficiency of 88.8%, high rate performance with 141 mA h g^{-1} at 10C, good cyclability with 81.1% capacity retention over 1000 cycles at 10C, and good low-temperature electrochemical properties with a reversible capacity of 235 mA h g^{-1} at −10 °C. In addition, the working mechanisms of this energy-storage material are systematically studied by various *in situ*, *ex situ* and variable-temperature characterization studies.

Experimental

Material preparation

The $Mo_4Nb_{26}O_{77}$ submicron-sized particles were prepared *via* a facile one-step solid-state reaction method. 3.809 mmol MoO_3 (99.5%, Macklin) and 9.222 mmol Nb_2O_5 (99.9%, Macklin) powders were well mixed and milled for 1 h by using a ball-milling machine (SPEX 8000M). The obtained powders were sintered at 700 °C for 4 h in air with a ramp rate of 10 °C min^{-1}.

Material characterization

The X-ray diffraction (XRD) test of the $Mo_4Nb_{26}O_{77}$ submicron-sized particles was carried out on an X-ray diffractometer (Rigaku Ultima IV) with Cu-Kα radiation in a 2θ range of 10°–70° at a scan rate of 10° min^{-1}. To obtain the exact lattice constants, a Rietveld refinement was conducted by using the free General Structure Analysis System (GSAS) program.[21] The *in situ* XRD tests were conducted based on a specially-designed electrochemical-cell module with a thin (0.2 mm) and low-X-ray-absorption Be window.[22] Field emission scanning electron microscopy (FESEM, JEOL JSM-7800F) and high-resolution transmission electron microscopy (HRTEM, JEOL JEM-2100) were used to record the morphologies, particle sizes and microstructures. *In situ* TEM on a specially-designed electrochemical holder was employed to observe the Li$^+$ insertion into the submicron-sized particles during lithiation and delithiation processes.[23] X-ray photoelectron spectroscopy (XPS, PHI5000 Versaprobe III) was employed to analyze the valences of the cations in the sample. At the liquid nitrogen temperature, N_2 adsorption–desorption isotherms were recorded on a surface area analyzer (ASAP 2460), from which the specific surface area was calculated using the Brunauer–Emmett–Teller (BET) model. An inductively coupled plasma atomic emission spectrometer (ICP-AES, Agilent ICPOES730) was used to determine the exact Mo : Nb molar ratio in $Mo_4Nb_{26}O_{77}$.

Electrochemical measurement

To investigate the electrochemical properties of the $Mo_4Nb_{26}O_{77}$ submicron-sized particles, coin cells of the CR2016 type were assembled in an Ar-filled glove box. Celgard® 2325 microporous polypropylene films served as separators. The counter electrodes were Li foil pieces. The electrolyte was 1 M $LiPF_6$ in a mixture of dimethyl carbonate, ethylene carbonate and diethylene carbonate in equal volumes. For the preparation of working electrodes, 70 wt% $Mo_4Nb_{26}O_{77}$, 20 wt% conductive carbon (Super-P® carbon) and 10 wt% polyvinylidene (PVDF) were mixed in *N*-methyl-2-pyrrolidone. Then, the slurry was coated on Cu-foil current collectors with a $Mo_4Nb_{26}O_{77}$ loading density of ∼1.0 mg cm^{-2}, which were fully dried at 110 °C in a vacuum. $LiMn_2O_4/Mo_4Nb_{26}O_{77}$ full cells were also assembled, in which $LiMn_2O_4$ (RDF15B, 99.9%) was purchased from Aladdin. The $LiMn_2O_4$ cathodes comprised 70 wt% $LiMn_2O_4$, 20 wt% Super-P® carbon and 10 wt% PVDF on Al-foil current collectors. The weight ratio between the anode and cathode materials was about 1 : 3.

The galvanostatic intermittent titration technique (GITT) and galvanostatic charge–discharge (GCD) tests were conducted on a multi-channel battery tester (CT-3008, Neware). The cyclic voltammetry (CV) tests were performed on an electrochemical workstation (CHI660E, Chenhua). The $Mo_4Nb_{26}O_{77}$/Li half cells were examined in a potential range of 0.8–3.0 V *vs.* Li/Li$^+$ and the $LiMn_2O_4/Mo_4Nb_{26}O_{77}$ full cells were examined in a voltage range of 1.0–3.2 V. The 1C current rate was 399 mA g^{-1}, corresponding to the large theoretical capacity of $Mo_4Nb_{26}O_{77}$ (399 mA h g^{-1}). The temperatures of the above electrochemical measurements were exactly controlled in a temperature-variable cryostat system (SPM-258, Ningbo Xinjiangnan). The practical capacities at different current rates and temperatures were calculated based on the weight of $Mo_4Nb_{26}O_{77}$.

19954 | *J. Mater. Chem. A*, 2022, **10**, 19953–19962

This journal is © The Royal Society of Chemistry 2022

Results and discussion

Crystal structure and morphology

The XRD pattern of $Mo_4Nb_{26}O_{77}$ matches well with a $W_4Nb_{26}O_{77}$-type crystal structure.[24] Its reasonable Rietveld refinement (small weighted profile residual of 0.0563) is shown in Fig. 1a, and its refined fractional atomic parameters are listed in Tables S1 and S2.† Even though its sintering temperature is much lower than other niobates due to the MoO_3 sintering aid (Fig. 1b and Table S3†), its XRD peaks are sharp and intense, indicating its high crystallinity. $Mo_4Nb_{26}O_{77}$ has a monoclinic shear ReO_3 crystal structure with a $C2$ space group (Fig. 1c). The lattice constants are refined to be $a = 29.76355(87)$ Å, $b = 3.82011(10)$ Å, $c = 26.00112(27)$ Å, $\beta = 92.377(4)°$, and $V = 2953.788(86)$ Å^3. The 4×4 and 3×4 Mo_6 ($M = Mo^{6+}$ and Nb^{5+} with an ion ratio of 1 : 13) octahedron-blocks alternately exist in the ac-layers at different levels, and infinitely expand along the b axis. The MO_6 octahedra are connected by corner- and edge-sharing, and the MoO_4 tetrahedra connect with the MO_6 octahedra by corner-sharing. As a result, an A–B–A layered structure with a large interlayer spacing (equal to the b value) and abundant open-tunnel-like vacant sites is formed, which enables the fast Li^+ diffusion and storage in $Mo_4Nb_{26}O_{77}$.[25,26] In addition, the MoO_4 tetrahedra can effectively anchor the MO_6 octahedra, undoubtedly contributing to the good structural stability of $Mo_4Nb_{26}O_{77}$.[27] The ICP-AES experiment reveals that the Mo : Nb molar ratio in $Mo_4Nb_{26}O_{77}$ is 3.98 : 26, which is in good agreement with its theoretical ratio (4 : 26).

The FESEM image of $Mo_4Nb_{26}O_{77}$ (Fig. 1d) clearly shows submicron-sized particles with different sizes averaging at ~200 nm. From the TEM image (Fig. 1e), rod shapes with different length-to-diameter ratios for the primary particles can be clearly seen. Based on its N_2 adsorption–desorption isotherms (Fig. 1f), its BET specific surface area is determined to be a relatively large value of 3.3 m^2 g^{-1}, which is the largest among all the reported niobates from solid-state reactions (Table S3†). The lattice fringe in the HRTEM image (Fig. 1g) is measured to be 0.375 nm, matching its (111) crystallographic plane. Moreover, the bright diffraction spots from the monocrystalline $Mo_4Nb_{26}O_{77}$ are presented in the SAED pattern (the inset of Fig. 1g), corresponding to its (003), (400) and (403) planes, which confirms its monoclinic shear ReO_3 structure ($C2$ space group). The EDX mapping images (Fig. S1†) reveal the uniformly distributed Mo, Nb and O in the tested region, thus verifying that the $Mo_4Nb_{26}O_{77}$ submicron-sized particles are of high purity and uniformity.
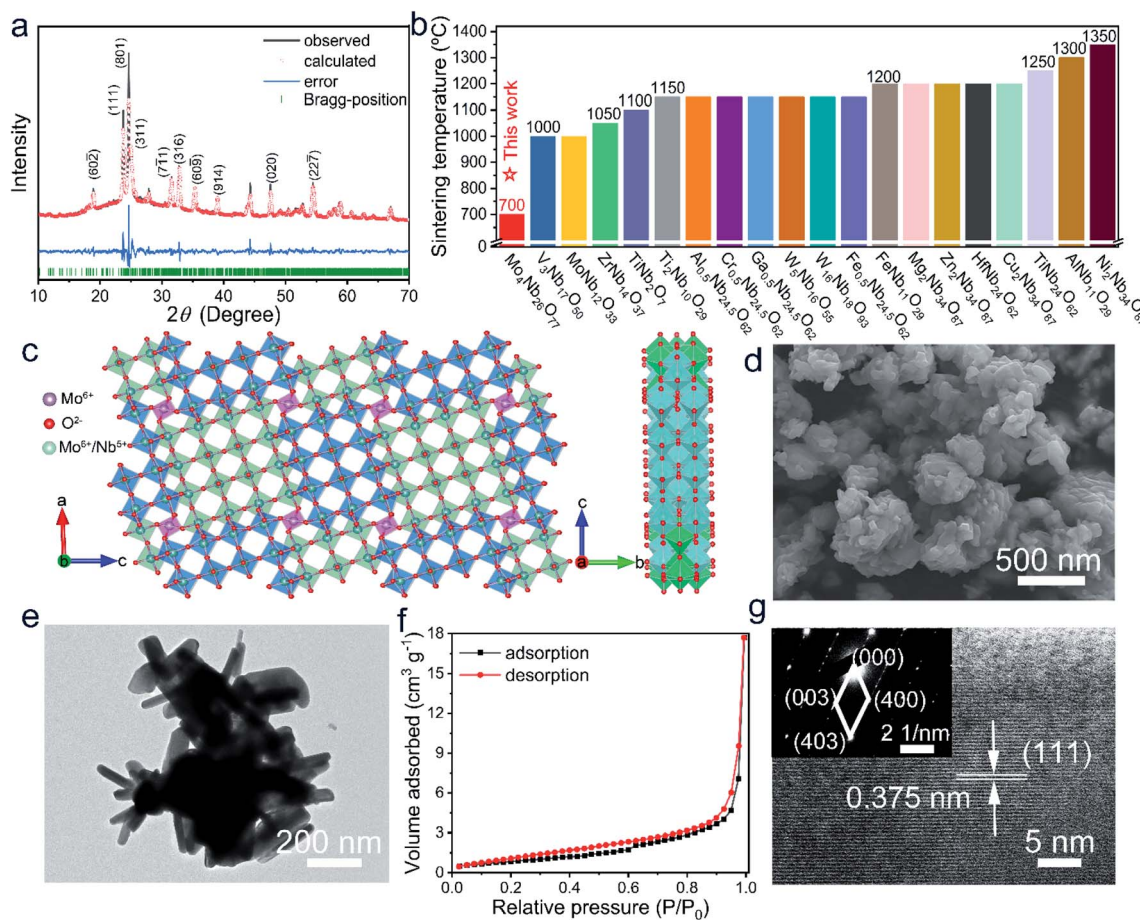

Fig. 1 Physico-chemical characterization studies of $Mo_4Nb_{26}O_{77}$. (a) Rietveld-refined XRD pattern. (b) Sintering temperature of $Mo_4Nb_{26}O_{77}$ from the solid-state reaction compared with other niobates. (c) Crystal structure viewed from different directions. (d) FESEM and (e) TEM images. (f) N_2 adsorption–desorption isotherms. (g) HRTEM image (inset: SAED pattern).

This journal is © The Royal Society of Chemistry 2022

J. Mater. Chem. A, 2022, **10**, 19953–19962 | **19955**

Temperature-dependent lithium-storage properties

The first four-cycle GCD curves of the $Mo_4Nb_{26}O_{77}$/Li half-cell at 0.1C and 25 °C are shown in Fig. 2a. In the first cycle, the discharge and charge capacities respectively reach 412 and 366 mA h g^{-1} with a high coulombic efficiency of 88.8% and an average working potential of 1.59 V. The reversible capacity of the $Mo_4Nb_{26}O_{77}$ submicron-sized particles is as large as 91.7% of the theoretical capacity, and is the largest in the field of niobate anode materials (Table S4†). In addition, the average working potential of $Mo_4Nb_{26}O_{77}$ is lower than typical niobate anode compounds, such as $TiNb_2O_7$ (1.64 V), $Ti_2Nb_{10}O_{29}$ (1.65 V) and $TiNb_{24}O_{62}$ (1.70 V).[27–30] Thus, the full cells with $Mo_4Nb_{26}O_{77}$ anodes have enhanced energy density.

$Mo_4Nb_{26}O_{77}$ further demonstrates reversible capacities of 295, 245, 209, 170 and 141 mA h g^{-1} respectively at 0.5C, 1C, 2C, 5C and 10C (Fig. 2b and c), suggesting its high rate performance. The reversible capacity at 10C remains at 81.1% over 1000 cycles (Fig. 2d), indicating that $Mo_4Nb_{26}O_{77}$ has good long-term cyclability.

The electrochemical properties of the $Mo_4Nb_{26}O_{77}$ submicron-sized particles are further investigated at a low temperature of −10 °C. Fig. 2e presents the first four-cycle GCD curves the $Mo_4Nb_{26}O_{77}$/Li half cell at 0.1C and −10 °C. The average working potential is slightly increased to 1.74 V but the initial coulombic efficiency is obviously increased to 97.1% compared with those at 25 °C. The reversible capacity at 0.1C is
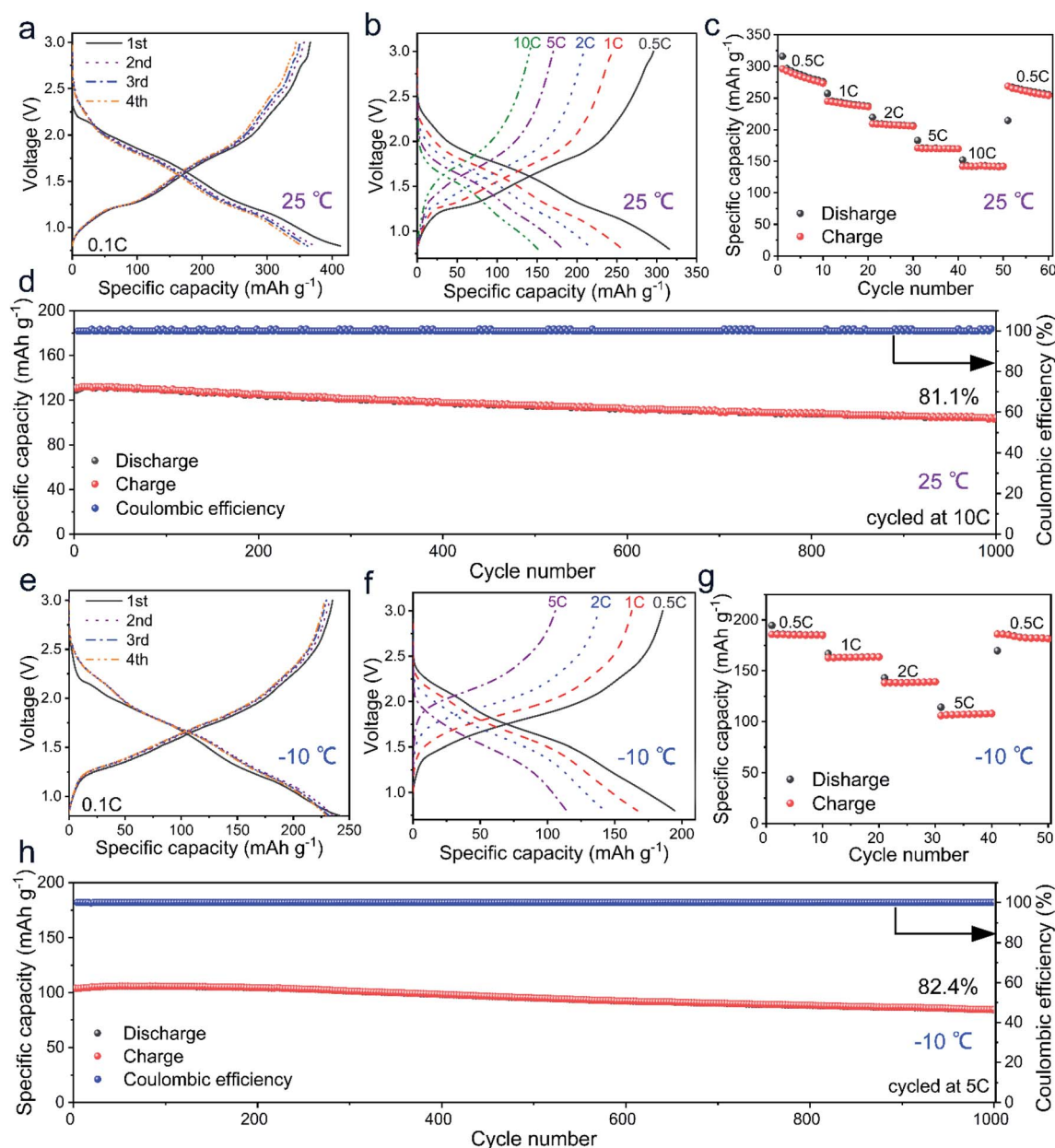

Fig. 2 Electrochemical characterization studies of the $Mo_4Nb_{26}O_{77}$/Li half cell at 25 and −10 °C. (a and e) First four-cycle GCD curves at 0.1C. (b and f) GCD curves at various current rates. (c and g) Rate performance. (d and h) Long-term cyclability over 1000 cycles.
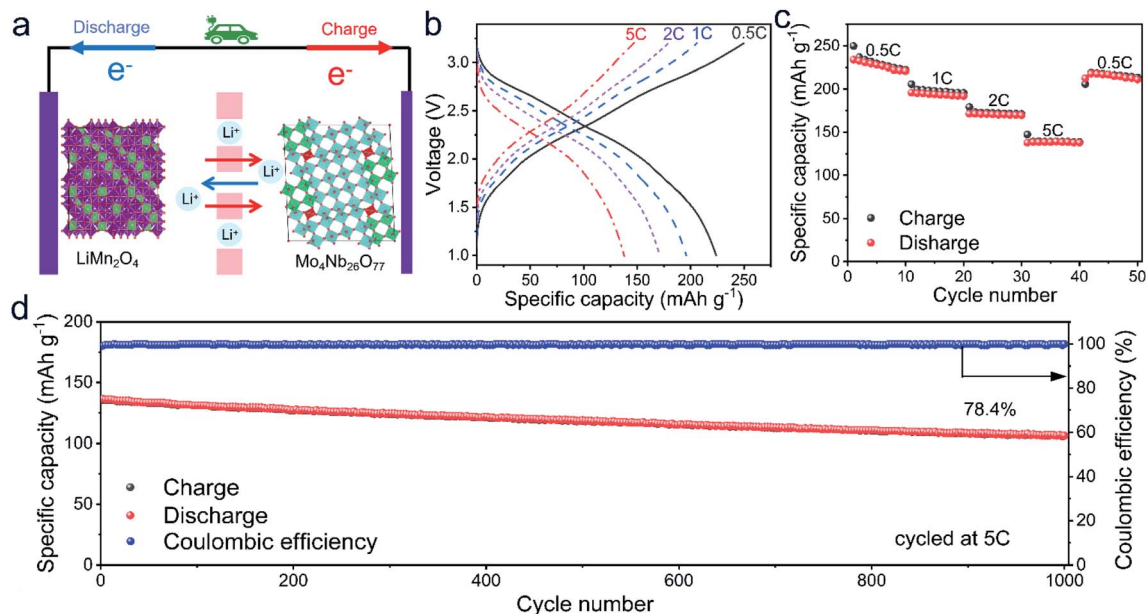
Fig. 3 Electrochemical properties of the $LiMn_2O_4/Mo_4Nb_{26}O_{77}$ full cell. (a) Schematic illustration of a full cell. (b) GCD curves at various current rates. (c) Rate performance. (d) Long-term cyclability over 1000 cycles at 5C.

235 mA h g^{-1}, maintaining 64.2% of that at 25 °C. At 0.5C, 1C, 2C and 5C, the capacities respectively drop to 185, 167, 138 and 114 mA h g^{-1} (Fig. 2f and g), which are 62.7, 68.1, 66.0 and 67.1% of those at 25 °C. However, the rate performance of $Mo_4Nb_{26}O_{77}$ at −10 °C is still high since the 5C vs. 0.5C capacity ratio at −10 °C (61.6%) is similar to that at 25 °C (57.6%). Additionally, $Mo_4Nb_{26}O_{77}$ still shows good long-term cyclability at −10 °C with 82.4% capacity retention over 1000 cycles at 5C (Fig. 2h).

A $LiMn_2O_4/Mo_4Nb_{26}O_{77}$ full cell (Fig. 3a) is also assembled to examine the practicability of $Mo_4Nb_{26}O_{77}$. It delivers 223, 193, 171 and 137 mA h g^{-1} at 0.5C, 1C, 2C and 5C, respectively (Fig. 3b and c). In addition, it is provided with 78.4% capacity retention over 1000 cycles at 5C (Fig. 3d). Clearly, the $Mo_4Nb_{26}O_{77}$ submicron-sized particles from the solid-state reaction in this work have a large reversible capacity, high initial coulombic efficiency, safe working potential, high rate performance and good long-term cyclability, and thereby can be a practical anode material for high-performance LIBs.

Redox mechanism and electrochemical kinetics

The CV profiles of the $Mo_4Nb_{26}O_{77}$/Li half cell at different temperatures are recorded and shown in Fig. 4a and b. The initial CV profile at a small sweep rate of 0.2 mV s^{-1} slightly differs from the subsequent profiles, which can be due to the irreversible polarization processes and/or the generation of thin SEI films.[22,31] After the initial cycle, however, the CV profiles exhibit good repeatability. At 25 °C, three cathodic/anodic peak-pairs are presented in the CV profiles, which are located at 2.25/2.29 V originating from the Mo^{5+}/Mo^{6+} redox couple, 1.61/1.71 V attributed to both the Mo^{4+}/Mo^{5+} and Nb^{4+}/Nb^{5+} couples, and

1.16/1.26 V rooted in the Nb^{3+}/Nb^{4+} couple.[32–34] The cathodic/anodic peak-pair at 1.16/1.26 V is intensive, indicating that many Nb^{4+} ions are reduced to Nb^{3+} ions during lithiation and that the average working potential of the $Mo_4Nb_{26}O_{77}$ submicron-sized particles is lowered, confirming the high electrochemical activity. In fact, at 0.1C, the reversible capacity of this $Mo_4Nb_{26}O_{77}$ material in the low-potential range of 1.5–0.8 V is up to 149 mA h g^{-1}, which surpasses those of the previously-reported niobate anode materials from solid-state reactions (Table S4†), thus significantly contributing to its very large reversible capacity of 366 mA h g^{-1} within 3.0–0.8 V. At −10 °C, the positions of these three peak-pairs slightly shift to 2.17/2.28 V, 1.62/1.81 V and 1.12/1.44 V, suggesting a slightly larger polarization than that at 25 °C. The CV peaks in the low potential region become weak due to the smaller capacity at −10 °C, which causes the slightly higher average working potential at −10 °C (Fig. 2e).

To further investigate the redox mechanism of the $Mo_4Nb_{26}O_{77}$ submicron-sized particles, the ex situ Mo-3d (Fig. 4c) and Nb-3d (Fig. 4d) XPS spectra are analyzed. In pristine $Mo_4Nb_{26}O_{77}$ at 25 °C, the characteristic peaks of Mo-3d$_{3/2}$ (236.59 eV), Mo-3d$_{5/2}$ (233.44 eV), Nb-3d$_{3/2}$ (210.49 eV) and Nb-3d$_{5/2}$ (207.71 eV) indicate that the valences of Mo and Nb are respectively +6 and +5, as expected.[33–36] After lithiation to 0.8 V, the characteristic peaks of Mo-3d$_{3/2}$ and Mo-3d$_{5/2}$ shift to lower binding energies of 232.60 and 229.45 eV, respectively, which match well with Mo^{4+}.[35] Meanwhile, the complicated Nb-3d$_{3/2}$ and Nb-3d$_{5/2}$ peaks are perfectly fitted by the combination of minor Nb^{4+} and major Nb^{3+}.[36] Therefore, all the Mo^{6+} ions are fully reduced to Mo^{4+}, and all the Nb^{5+} ions are reduced to Nb^{4+} or Nb^{3+}. After delithiation to 3.0 V, the binding energies of all
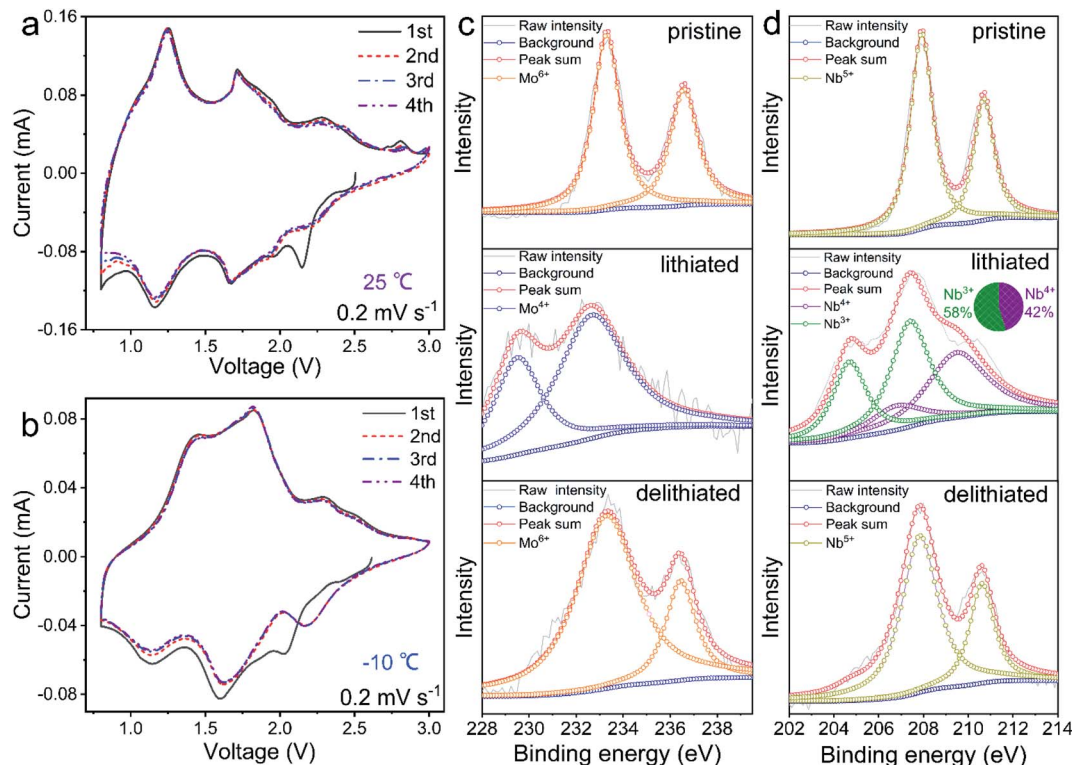
Fig. 4 Redox mechanism of $Mo_4Nb_{26}O_{77}$ submicron-sized particles. First four-cycle CV profiles of the $Mo_4Nb_{26}O_{77}$/Li half cell at (a) 25 and (b) −10 °C. *Ex situ* (c) Mo-3d and (d) Nb-3d XPS spectra of pristine, lithiated and delithiated $Mo_4Nb_{26}O_{77}$ samples at 25 °C.

the peaks almost recover their original values, suggesting the excellent reversibility of the redox reaction based on the Mo^{5+}/ Mo^{6+}, Mo^{4+}/Mo^{5+}, Nb^{4+}/Nb^{5+} and Nb^{3+}/Nb^{4+} couples. These desirable valence variations confirm the multiple-electron transfer per Mo/Nb in $Mo_4Nb_{26}O_{77}$ and explain its large reversible capacity.

To study the electrochemical kinetics of the $Mo_4Nb_{26}O_{77}$ submicron-sized particles, the CV profiles at 0.4, 0.7 and 1.1 mV s^{-1} are also recorded at 25 °C (Fig. 5a) and −10 °C (Fig. 5b). At 25 °C, by increasing the sweep rate, the CV peaks show only slight shifts, demonstrating the low polarization and further confirming the high electrochemical activity of the $Mo_4Nb_{26}O_{77}$ submicron-sized particles. The analysis of these CV profiles is based on the equation of $I = av^b$, in which I and v are the peak current and sweep rate, respectively, and a and b are variable parameters at different potentials.[37,38] The $b = 1$ case corresponds to the situation where lithiation and delithiation are fully controlled by capacitive behavior, whereas the $b = 0.5$ case indicates that the diffusion-controlled behavior is completely dominant. In our $Mo_4Nb_{26}O_{77}$ case, the b values for the cathodic and anodic peaks at 25 °C are both 0.83, while those at −10 °C are increased to 0.88 and 0.98, respectively (Fig. 5c). Clearly, the capacitive process significantly contributes to the lithium storage within the $Mo_4Nb_{26}O_{77}$ submicron-sized particles at different temperatures, which can be ascribed to not only the large interlayer spacing of $Mo_4Nb_{26}O_{77}$ but also the large specific surface area of this material.[39] The fact that the

capacitive process plays a more important role at −10 °C is very reasonable since the low-temperature Li^+ diffusion is undoubtedly slower (see the following Fig. 5e).[22]

The GITT experiments of the $Mo_4Nb_{26}O_{77}$/Li cell with a ten-minute pulse current at 0.1C between twenty-minute rest intervals were conducted for investigating the Li^+ diffusivity of the $Mo_4Nb_{26}O_{77}$ submicron-sized particles,[26] and the results for the first two cycles at 25 and −10 °C are revealed in Fig. 5d and e, respectively. The apparent Li^+ diffusion coefficients (D_{Li}) of $Mo_4Nb_{26}O_{77}$ at different states of discharge/charge and temperatures are determined based on Fick's second law (eqn (S1), (S2) and Fig. S2, detailed in ESI†).[40] At 25 °C, the average D_{Li} values in the first and second lithiation/delithiation processes reach 1.95×10^{-11}/1.93×10^{-11} and 2.09×10^{-11}/1.89×10^{-11} cm^2 s^{-1}, respectively. At −10 °C, the corresponding values decrease by roughly a half, showing 9.66×10^{-12}/8.16×10^{-12} and 9.43×10^{-12}/7.84×10^{-12} cm^2 s^{-1}. The Li^+ diffusivity of $Mo_4Nb_{26}O_{77}$ (even at −10 °C) is faster than that of most niobate anode materials from a solid-state reaction at 25 °C (Table S5†), which is due to not only its open shear ReO_3 crystal structure with plenty of tunnels conducive to Li^+ transport and storage but also its submicron-sized rod morphology with short sidewall-to-axis distances for Li^+ transport.[41] The fast Li^+ diffusivity of $Mo_4Nb_{26}O_{77}$ together with its relatively large electrochemical-reaction area undoubtedly contributes to its good electrochemical properties (especially its high rate performance) at different temperatures.
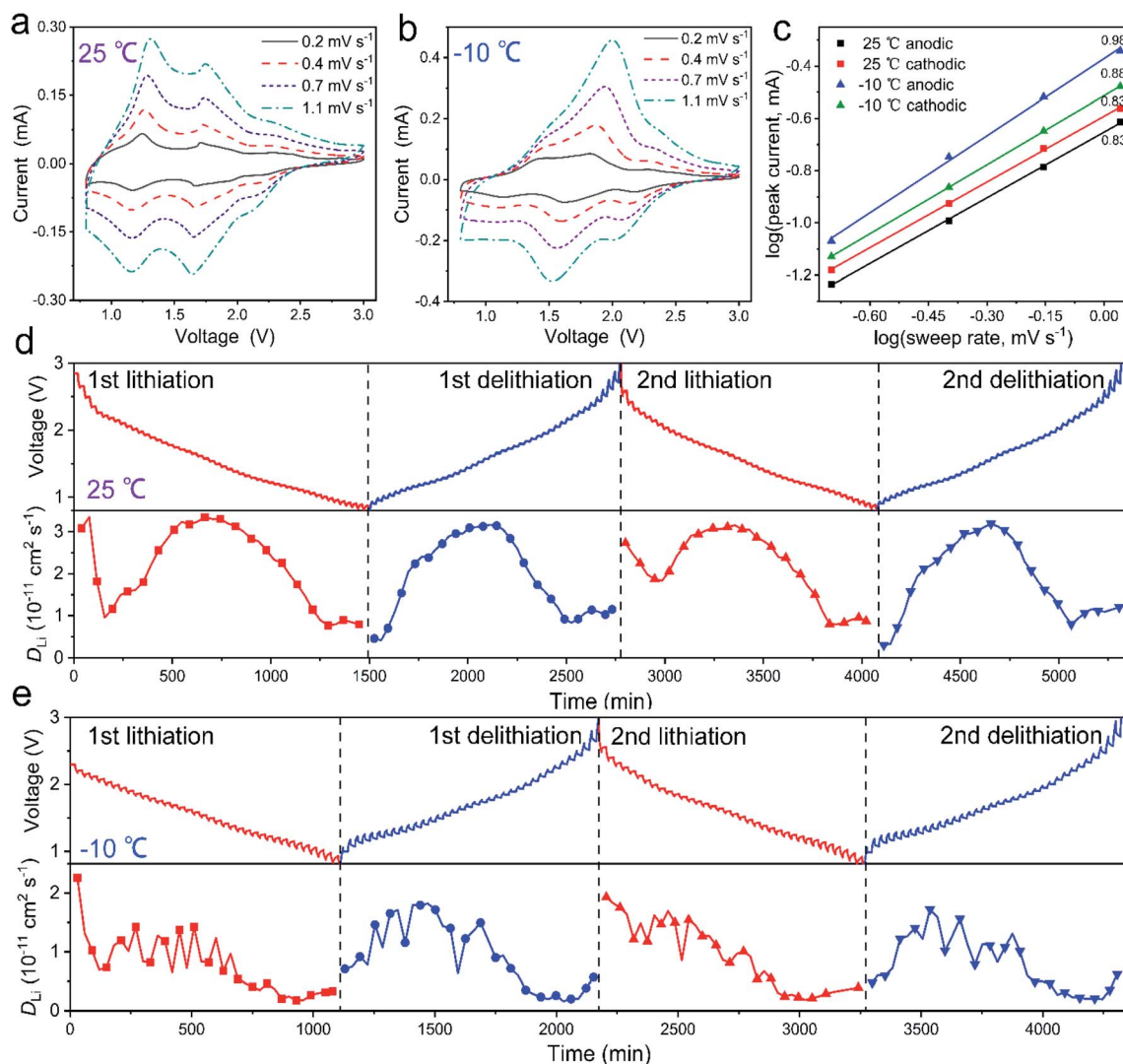
19958 | *J. Mater. Chem. A*, 2022, **10**, 19953–19962

This journal is © The Royal Society of Chemistry 2022

Fig. 5 Electrochemical kinetics of $Mo_4Nb_{26}O_{77}$ submicron-sized particles. CV profiles of the $Mo_4Nb_{26}O_{77}$/Li half cell at (a) 25 and (b) −10 °C at different sweep rates. (c) Linear relationship between log(current) and log(sweep rate). GITT curves and variations in Li$^+$ diffusion coefficients (first two cycles) at (d) 25 and (e) −10 °C.

Crystal-structure evolution and the lithium-storage mechanism

In order to understand the lithium-storage mechanism of the $Mo_4Nb_{26}O_{77}$ submicron-sized particles, the crystal-structure evolution during the electrochemical reaction is analyzed based on *in situ* XRD at 25 and −10 °C.[42–45] Fig. 6a and b show the first-three-cycle two-dimensional and pristine *in situ* XRD patterns recorded at 0.4C and 25 °C with GCD curves, respectively. During the initial lithiation, all the XRD peaks show decreased intensities since the insertion of Li$^+$ within the $Mo_4Nb_{26}O_{77}$ lattice undoubtedly decreases the lattice order.[46] The XRD peaks of the (111), (311), (511), (316) and (020) planes monotonically shift towards lower Bragg angles, suggesting that the lattice spacings of these planes monotonically increase. However, the XRD peak of the (801) plane shifts towards larger Bragg angles until ∼1.1 V and then slowly shifts towards lower Bragg angles, indicating that the variation of its lattice spacing

is complicated. During the subsequent delithiation, all these XRD peaks almost recover their original intensities and positions. The variation trends of all the XRD peaks during the subsequent second and third cycles are almost the same as those during the initial cycle. Therefore, $Mo_4Nb_{26}O_{77}$ is an intercalation-type anode compound with good crystal-structure reversibility and stability during lithiation/delithiation.

Through Rietveld-refining the *in situ* XRD patterns, the reversible variations of lattice constants (a, b, c, β and V) during lithiation/delithiation are revealed (Fig. 6c). When the *in situ* half cell is discharged to 0.8 V, the variations in the a, b, c, β and V values are −1.89, +11.7, +1.01, +1.28 and +12.8% (*vs.* the pristine values), respectively, matching with the *ex situ* HRTEM result (Fig. 6d) that the (111) lattice spacing enlarges from 0.375 nm at the pristine state (OCV) to 0.407 nm at the lithiated state (0.8 V) and then restores 0.375 nm at the delithiated state (3.0 V).
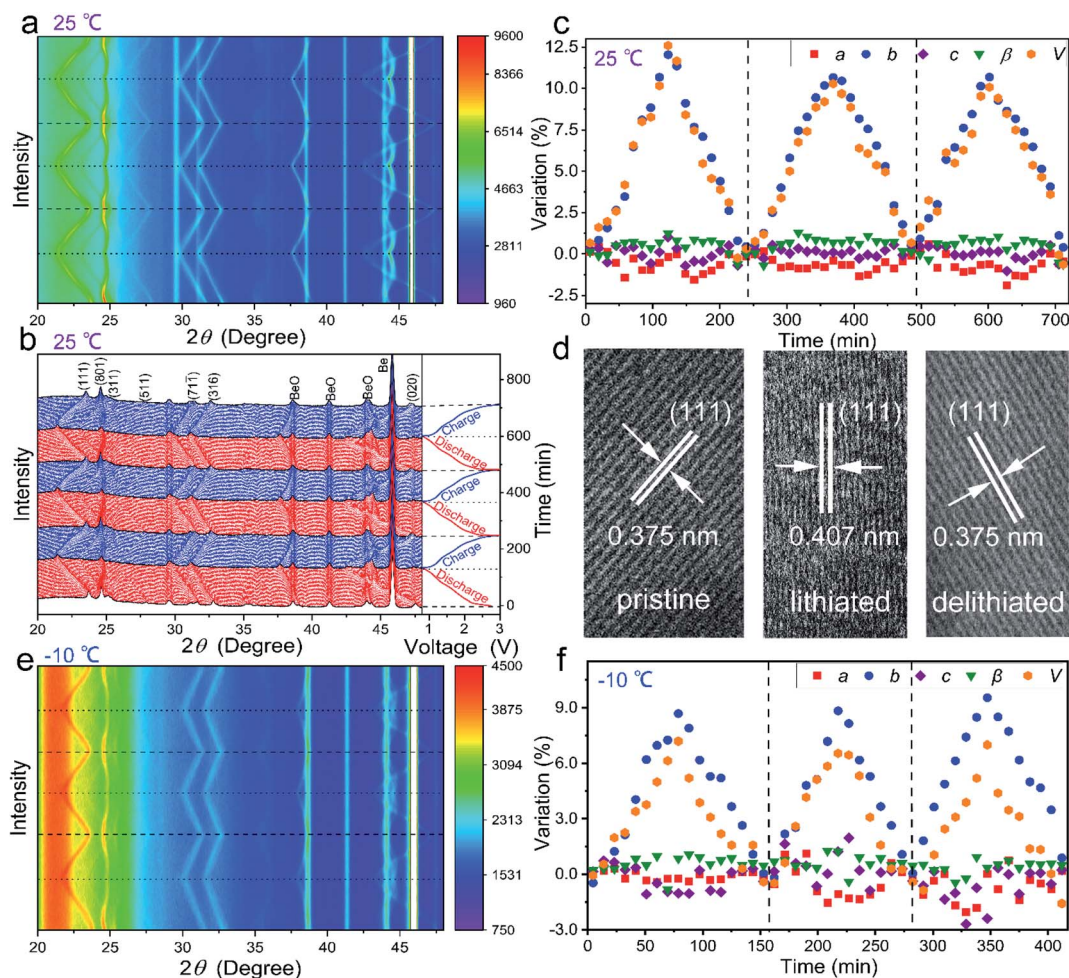
This journal is © The Royal Society of Chemistry 2022

J. Mater. Chem. A, 2022, **10**, 19953–19962 | **19959**

Fig. 6 Crystal-structure evolution of $Mo_4Nb_{26}O_{77}$ submicron-sized particles. (a) Two-dimensional and (b) pristine *in situ* XRD patterns of the $Mo_4Nb_{26}O_{77}$/Li half cell (25 °C) recorded at 0.4C (first three cycles) with GCD curves. (c) Variations in lattice constants of $Mo_4Nb_{26}O_{77}$ at 25 °C (first three cycles). (d) *Ex situ* HRTEM images of pristine, lithiated and delithiated $Mo_4Nb_{26}O_{77}$ samples. (e) Two-dimensional *in situ* XRD patterns of the $Mo_4Nb_{26}O_{77}$/Li half cell (−10 °C) recorded at 0.4C (first three cycles). (f) Variations in lattice constants of $Mo_4Nb_{26}O_{77}$ at −10 °C (first three cycles).

The *in situ* XRD experiment is further carried out at −10 °C, and the results show that the variation trend of all the XRD peaks is similar to that at 25 °C (Fig. 6e), but the peak shifts and the lattice-constant variations are smaller than those at 25 °C (Fig. 6f). At 0.8 V, the variations in the *a*, *b*, *c*, *β* and *V* values are −1.53, +9.53, −1.03, +1.23 and +7.18% (*vs.* the pristine values), respectively. The decrease in the maximum unit-cell-volume variation is very reasonable due to the smaller reversible capacity (fewer Li^+ ions inserted) at the low temperature. The unit-cell-volume variations of $Mo_4Nb_{26}O_{77}$ in the two cases at different temperatures are very limited, which significantly contributes to its good cyclability in the broad temperature range. In addition, both the cases show that the monotonical *V*-value increase is mainly determined by the monotonical *b*-value increase during lithiation, suggesting that the inserted Li^+ ions are mainly stored within the interstices between the (010) planes of $Mo_4Nb_{26}O_{77}$.

Advanced *in situ* TEM technology is employed to further study the crystal-structure and morphology evolution of the

$Mo_4Nb_{26}O_{77}$ submicron-sized particles. The schematic diagram of the *in situ* TEM experiment is illustrated in Fig. 7a.[23] The working electrode is $Mo_4Nb_{26}O_{77}$ submicron-sized particles coated on an Ag rod. Li metal coated on a W rode is used as the Li source and counter electrode. A naturally grown Li_2O coating on the Li-metal surface serves as the solid electrolyte. An additional voltage of 3.0 V is applied to drive the Li → Li_2O → $Mo_4Nb_{26}O_{77}$ lithiation process. The comparison of the *in situ* SAED patterns recorded at the pristine and lithiated states (Fig. 7b and c) reveals little change in the lattice spacings of the (401), (202) and (603) planes, verifying the small *a* and *c* variations. The strain fringes arising from the Li^+ insertion into the $Mo_4Nb_{26}O_{77}$ lattice show significant movement as highlighted in Fig. 7d–f (also see the ESI Video†), verifying the high electrochemical activity of the $Mo_4Nb_{26}O_{77}$ submicron-sized particles.[47,48] However, the morphology and volume variations are rather small, which confirms the intercalation nature of $Mo_4Nb_{26}O_{77}$ with small unit-cell-volume change.

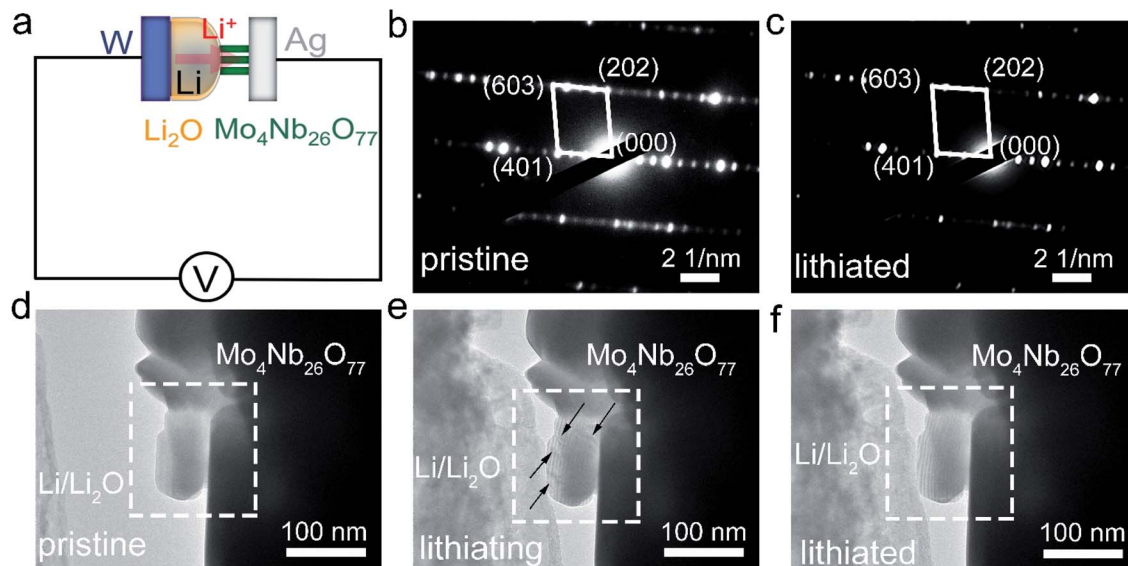**19960** | *J. Mater. Chem. A*, 2022, **10**, 19953–19962

This journal is © The Royal Society of Chemistry 2022

Fig. 7 *In situ* TEM characterization of $Mo_4Nb_{26}O_{77}$ submicron-sized particles. (a) Schematic illustration of the *in situ* TEM half cell. *In situ* SAED patterns recorded at (b) pristine and (c) lithiated states. *In situ* TEM images of $Mo_4Nb_{26}O_{77}$ recorded at (d) pristine, (e) lithiating and (f) lithiated states. Significant movement of strain fringes induced by Li^+ insertion is observed within white and dotted rectangles.

Conclusions

We use MoO_3 as the sintering aid and Mo source for the preparation of the $Mo_4Nb_{26}O_{77}$ anode material with submicron-sized primary particles. The resultant high electrochemical activity together with the highly reversible redox reaction of the multiple Mo^{5+}/Mo^{6+}, Mo^{4+}/Mo^{5+}, Nb^{4+}/Nb^{5+} and Nb^{3+}/Nb^{4+} couples enables a large practical capacity of 366 mA h g^{-1} (0.1C, 91.7% of the theoretical one) at a relatively low average working potential of 1.59 V at 25 °C, a satisfactory capacity of 235 mA h g^{-1} (0.1C, 64.2% of that at 25 °C) at −10 °C, and high initial coulombic efficiencies of 88.8% at 25 °C and 97.1% at −10 °C. $Mo_4Nb_{26}O_{77}$ has an open and stable shear ReO_3 crystal structure, significantly contributing to its fast Li^+ diffusivity and small unit-cell-volume change during the storage of most Li^+ ions within the interstices between its (010) planes. Consequently, high rate performance with 5C *vs.* 0.5C capacity ratios of 57.6% at 25 °C and 61.6% at −10 °C is achieved, and advanced cyclability with a capacity retention of 81.1% (10C) at 25 °C and 82.4% (5C) at −10 °C over 1000 cycles is obtained. These good electrochemical properties of our $Mo_4Nb_{26}O_{77}$ material at different temperatures prove its great application potential in high-performance LIBs. Our modification of the solid-state reaction method through using sintering aids with redox activity is general, and can be applied to other energy-storage materials for enhancing their electrochemical activity and energy density.

Conflicts of interest

There are no conflicts of interest to declare.

Acknowledgements

Notes and references

1 C. Zhao, Q. Wang, Z. Yao, J. Wang, B. Sanchez-Lengeling, F. Ding, X. Qi, Y. Lu, X. Bai, B. Li, H. Li, A. Aspuru-Guzik, X. Huang, C. Delmas, M. Wagemaker, L. Chen and Y. Hu, *Science*, 2020, **370**, 708.

2 Y. Bi, J. Tao, Y. Wu, L. Li, Y. Xu, E. Hu, J. Hu, C. Wang, J. Zhang, Y. Qi and J. Xiao, *Science*, 2020, **370**, 13173.

3 W. Zhang, D. Seo, T. Chen, L. Wu, M. Topsakai, Y. Zhu, D. Lu, G. Ceder and F. Wang, *Science*, 2020, **367**, 1030.

4 H. Liu, Z. Zhu, Q. Yan, S. Yu, X. He, Y. Chen, R. Zhang, L. Ma, T. Liu, M. Li, R. Lin, Y. Chen, Y. Li, X. Xing, Y. J. Choi, L. Gao, H. S. Cho, K. An, J. Feng, R. Kostecki, K. Amine, T. Wu, J. Lu, H. Xin, S. P. Ong and P. Liu, *Nature*, 2020, **585**, 63.

5 J. Zhao, D. Wei, C. Zhang, Q. Shao, V. Murugadoss, Z. Guo, Q. Jiang and X. Yang, *Eng. Sci.*, 2021, **15**, 1.

6 K. J. Griffith, K. M. Wiaderek, G. Cibin, L. E. Marbella and C. P. Grey, *Nature*, 2018, **559**, 556.

7 X. Zhang, N. Peng, T. Liu, R. Zheng, M. Xia, H. Yu, S. Chen, M. Shui and J. Shu, *Nano Energy*, 2019, **65**, 104049.

8 J. Liao, W. Ni, C. Wang and J. Ma, *Chem. Eng. J.*, 2020, **391**, 123489.

9 Q. Deng, Y. Fu, C. Zhu and Y. Yu, *Small*, 2019, **15**, 180488.

10 H. Sun, L. Mei, J. Liang, Z. Zhao, C. Lee, H. Fei, M. Ding, J. Lau, M. Li, C. Wang, X. Xu, G. Hao, B. Papandrea, I. Shakir, B. Dunn, Y. Huang and X. Duan, *Science*, 2017, **356**, 599.

11 C. Hou, B. Wang, V. Murugadoss, S. Vupputuri, Y. Chao, Z. Guo, C. Wang and W. Du, *Eng. Sci.*, 2020, **11**, 19.

12 M. Culebras, G. A. Collins, A. Beaucamp, H. Geaney and M. N. Collins, *Eng. Sci.*, 2022, **17**, 195.

13 J. Guan, Y. Li, Y. Guo, R. Su, G. Gao, H. Song, H. Yuan and B. Liang, *ACS Sustainable Chem. Eng.*, 2017, **5**, 1026.

14 C. Lai, Y. Wang, L. Fu, H. Song, B. Liu, D. Pan, Z. Guo, I. Seok, K. Li and H. Zhang, *Adv. Compos. Hybrid Mater.*, 2021, **4**, 543.

15 Y. Zhang, Y. An, L. Wu, H. Chen, Z. Li, H. Dou, V. Murugadoss, J. Fan, X. Zhang, X. Mai and Z. Guo, *J. Mater. Chem. A*, 2019, **7**, 19668.

16 X. Dong, X. Zhao, Y. Chen and C. Wang, *Adv. Compos. Hybrid Mater.*, 2021, **4**, 1070.

17 J. Han, Y. Huang and J. B. Goodenough, *Chem. Mater.*, 2011, **23**, 2027.

18 X. Hu, W. Zhang, X. Liu, Y. Mei and Y. Huang, *Chem. Soc. Rev.*, 2015, **44**, 2376.

19 Q. Deng, Y. Fu, C. Zhu and Y. Yu, *Small*, 2019, **15**, 1804884.

20 S. R. Sivakkumar, J. Y. Nerkar and A. G. Pandolfo, *Electrochim. Acta*, 2010, **55**, 3330.

21 B. H. Toby, *J. Appl. Crystallogr.*, 2001, **34**, 210.

22 T. Jiang, S. Ma, J. Deng, T. Yuan, C. Lin and M. Liu, *Adv. Sci.*, 2022, **9**, 105119.

23 Y. Zhang, J. Liu and H. Wang, *Sci. China: Technol. Sci.*, 2019, **62**, 546.

24 A. F. Fuentes, A. M. DelaCruz and L. M. Martinez, *Solid State Ionics*, 1996, **92**, 103.

25 Q. Fu, R. Li, X. Zhu, G. Liang, L. Luo, Y. Chen, C. Lin and X. Zhao, *J. Mater. Chem. A*, 2019, **7**, 19862.

26 L. Yang, X. Zhu, X. Li, X. Zhao, K. Pei, W. You, X. Li, Y. Chen, C. Lin and R. Che, *Adv. Energy Mater.*, 2019, **9**, 1902174.

27 G. Li, X. Wang and X. Ma, *J. Mater. Chem. A*, 2013, **1**, 12409.

28 X. Wu, S. Lou, X. Cheng, C. Lin, J. Gao, Y. Ma, P. Zuo, C. Du, Y. Gao and G. Yin, *ACS Appl. Mater. Interfaces*, 2018, **10**, 27056.

29 Q. Cheng, J. Liang, Y. Zhu, L. Si, C. Guo and Y. Qian, *J. Mater. Chem. A*, 2014, **2**, 17258.

30 Q. Zhu, J. Jiang, Z. Li, Y. Xu, H. Dou and X. Zhang, *Electrochim. Acta*, 2021, **388**, 138656.

31 X. Lu, Z. Jian, Z. Fang, L. Gu, Y. Hu, W. Chen, Z. Wang and L. Chen, *Energy Environ. Sci.*, 2011, **4**, 2638.

32 C. T. Cherian, M. V. Reddy, S. C. Haur and B. V. R. Chowdari, *ACS Appl. Mater. Interfaces*, 2013, **5**, 918.

33 R. Li, G. Liang, X. Zhu, Q. Fu, Y. Chen, L. Luo and C. Lin, *Energy Environ. Mater.*, 2020, **4**, 65.

34 X. Zhu, J. Xu, Y. Luo, Q. Fu, G. Liang, L. Luo, Y. Chen, C. Lin and X. Zhao, *J. Mater. Chem. A*, 2019, **7**, 6522.

35 L. Benoist, D. Gonbeau, G. Guillouzo, E. Schmidt, G. Meunier and A. Levasseur, *Solid State Ionics*, 1995, **76**, 81.

36 G. Thornton, A. F. Orchard and C. N. R. Rao, *Phys. Lett. A*, 1975, **54**, 235.

37 V. Augustyn, J. Come, M. A. Lowe, J. W. Kim, P. L. Taberna, S. H. Tolbert, H. D. Abruna, P. Simon and B. Dunn, *Nat. Mater.*, 2013, **12**, 518.

38 V. Augustyn, P. Simon and B. Dunn, *Energy Environ. Sci.*, 2014, **7**, 1597.

39 X. Zhu, Q. Fu, L. Tang, C. Lin, J. Xu, G. Liang, R. Li, L. Luo and Y. Chen, *ACS Appl. Mater. Interfaces*, 2018, **10**, 23711.

40 A. J. Bard and L. R. Faulkner, *Electrochemical Methods: Fundamentals and Applications*, Wiley, 2nd edn, 2001.

41 X. Zhu, H. Cao, R. Li, Q. Fu, G. Liang, Y. Chen, L. Luo, C. Lin and X. Zhao, *J. Mater. Chem. A*, 2019, **7**, 25537.

42 X. Lu, H. Liu, V. Murugadoss, I. Seok, J. Huang, J. E. Ryu and Z. Guo, *Eng. Sci.*, 2020, **9**, 25.

43 J. Huang, Y. Luo, M. Weng, J. Yu, L. Sun, H. Zeng, Y. Liu, W. Zeng, Y. Min and Z. Guo, *ES Mater. Manuf.*, 2021, **13**, 23.

44 X. Hu, H. Wu, X. Lu, S. Liu and J. Qu, *Adv. Compos. Hybrid Mater.*, 2021, **4**, 478.

45 Y. Xie, Y. Yang, Y. Liu, S. Wang, X. Guo and H. Wang, *Adv. Compos. Hybrid Mater.*, 2021, **4**, 543.

46 G. Liang, L. Yang, Q. Han, G. Chen, C. Lin, Y. Chen, L. Luo, X. Liu, Y. Li and R. Che, *Adv. Energy Mater.*, 2020, **10**, 1904267.

47 P. Wu, X. Xu, Y. Wu, F. Xu, X. Wang, J. Meng, C. Han, X. Liu, Z. Zhu and L. Mai, *Adv. Energy Mater.*, 2021, **11**, 2003612.

48 L. Yang, G. Liang, H. Cao, S. Ma, X. Liu, X. Li, G. Chen, W. You, C. Lin and R. Che, *Adv. Funct. Mater.*, 2022, **32**, 2105026.